Optik - International Journal for Light and Electron Optics 191 (2019) 80–88

Contents lists available at ScienceDirect

Optik

journal homepage: www.elsevier.com/locate/ijleo

Original research article

Study of the impact of co-phasing errors for segmented primary mirror using nonlinear analysis

Huisheng Yang[a,b,*], Xuejun Zhang[a], Zhilai Li[a], Xiaokun Wang[a], Mengmeng Xu[a]

[a] Changchun Institute of Optics, Fine Mechanics and Physics, Chinese Academy of Sciences, Changchun, 130033, China
[b] University of Chinese Academy of Sciences, Beijing, 100049, China

ARTICLE INFO

Keywords:
Ultra large aperture
Space-based telescope
Segmented primary mirror
Co-phasing error
Wavefront deformation

ABSTRACT

Segmented primary mirror, which is the prerequisite for space telescope with aperture beyond 4 m, is very sensitive to co-phasing errors stemming from segment position and attitude errors as well as aspheric parameter errors. These errors are random and therefore difficult to correct, which can result in image quality degradation. In order to investigate the impacts of the co-phasing errors, a nonlinear calculation method of wavefront deformation is proposed through ray tracing, and numerical simulations are accomplished to analyze the impact of all these errors. The simulation results show that random co-phasing error will lead to uncertain wavefront deformation, which can be estimated using the Monte Carlo simulation. When the error limits are small enough, the wavefront deformation caused by definite or random co-phasing errors approximately obey the linearity theorem, and the total deformation is the root sum square of wavefront deformations generated by all single co-phasing errors.

1. Introduction

To meet the requirements of astronomy observation, astronomers need to go further, explore, discover and study more distant and faint planet, which means building telescopes with larger aperture for greater light-gather power and spatial resolution [1,2]. The study from National Aeronautics and Space Administration (NASA) shows that the discovery speed of earth-like planets is directly proportional to the 1.8th power of the aperture diameter D and the 0.4th power of the time t, thus a telescope with aperture larger than 8 m is necessary to meet the basic requirements of astronomy observation [3,4]. Space-based telescopes are immune to the effects of earth atmosphere and diurnal thermal cycling compared with ground-based telescopes, and can achieve diffraction-limited imaging. This outstanding advantage fascinates astronomers. However, space-based telescope with aperture larger than 4 m should adopt the segmented and deployable primary mirror (PM) because of the limitation from the launch vehicle fairing [5–7]. In order to achieve this target, several programs using segmented PM are being implemented, which include the James Webb Space Telescope (JWST) [8], the Advanced Technology Large Aperture Space Telescope (ATLAST) [9] and the Thirty Meter Space Telescope (TMST) [10].

When segments with correct aspheric parameters are properly phased relative to each other, they act as a single mirror [11]. Limited by the precision of positioning mechanism, segments will inevitably contain six degree of freedom (DOF) pose errors (including three DOF position errors and three DOF attitude errors) after PM co-phasing. Additionally, the optical parameter errors deriving from fabrication will also bring significant wavefront deformation (WD). All these errors will result in image quality degradation. At present, the research on segment co-phasing error mainly focuses on the error detection [12–15]. The analysis of WD

* Corresponding author at: Changchun Institute of Optics, Fine Mechanics and Physics, Chinese Academy of Sciences, Changchun, 130033, China.
E-mail address: yanghuisheng@126.com (H. Yang).

https://doi.org/10.1016/j.ijleo.2019.05.104
Received 20 March 2019; Accepted 31 May 2019

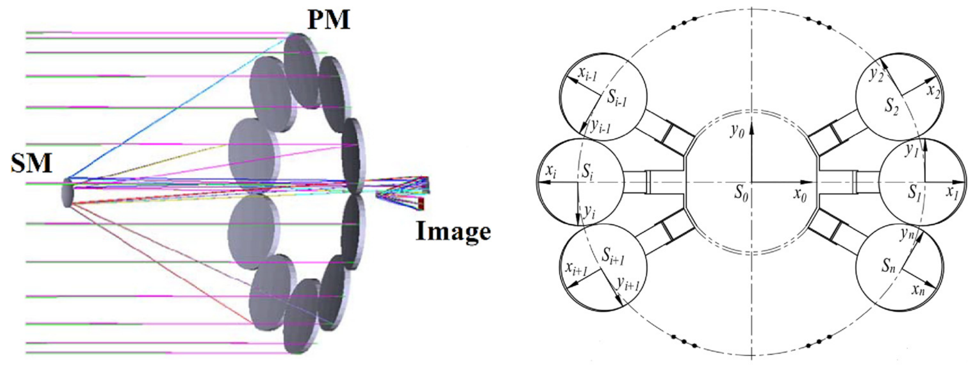

(a) optical system (b) segmented primary mirror

Fig. 1. Optical design of an 8 m space telescope.

caused by random aspheric parameter and pose errors is rarely concerned. Piston and tip/tilt errors with definite value defined in PM coordinate system have been analyzed by Ref. [16–22]. They cannot resolve the impact of errors with random value and the errors defined in segments coordinate system neither.

This paper proposes a nonlinear method for calculating the WD stemming from segments random pose and parameter errors. Firstly, we introduced the basic composition of a segmented PM with 8 m aperture. The sources of the random co-phasing errors are then presented. The WD caused by these errors is analyzed through rays tracing. Finally, numerical simulations are carried out to verify the theoretical equations. This work can provide a theoretical basis and data support for segmented telescope design and fabrication.

2. Segmented primary mirror

The optical architecture of a space observatory with 8 m segmented PM is illustrated in Fig. 1. Its optical design is a three mirror anastigmat (TMA), with four optical surfaces: the segmented PM, secondary mirror (SM), tertiary mirror (TM), and the folding mirror. The PM consists of 10 circular segments. Each segment is 1.9 m in diameter, and has identical aspheric parameters (radius of curvature $R = 10m$ and conic constant $k = -1$). When properly phased relative to each other, these segments act as a single mirror, and can provide an aperture of approximate 8 m for observatory. This operation is achieved in the segment coordinate system $\{S_i\}$ (Fig. 1(b)) by six DOF rigid body motions of each segment.

3. Sources of co-phasing errors

The PM co-phasing errors mainly include segment aspheric parameter errors originating from fabrication errors, and segment pose errors caused by six DOF positioning errors.

3.1. Aspheric parameter errors

Segments are grinded, ground and polished successively to obtain the optical surface meeting requirements. Different testing methods are used in different stages to ensure machining accuracy. Interference testing is used in the polishing stage, and profilometer testing was used in other stages. Segment prescription errors mainly originate from test errors in manufacture, as the manufacture precision is greater than the corresponding testing accuracy. The prescription errors are mainly produced in profilometer testing, because the material removal is so little in polishing process that it cannot change segment surface-shape. The profilometer testing consists of two stages. Firstly, the coordinate values of discrete points on the segment surface are measured, and then aspheric parameters are calculated using least square method. Therefore, the prescription error is the function of the measurement errors of all the points. According to the central limit theorem (CLT), the segment prescription errors approximately follow multidimensional independent normal distribution:

$$\Delta R \sim \mathrm{N}(0, \sigma_R^2); \Delta k \sim \mathrm{N}(0, \sigma_k^2) \tag{1}$$

where ΔR is the paraxial radius error of curvature. Δk is the conic constant error. σ^R is the standard deviation of ΔR. σ^k is the standard deviation of Δk.

3.2. Pose errors

In order to fit the rocket faring, the PM must be folded and then deployed in space. Limited by the precision of deployable mechanism, the segments will inevitably contain six DOF pose errors after deployment. For the segmented PM with conic-section

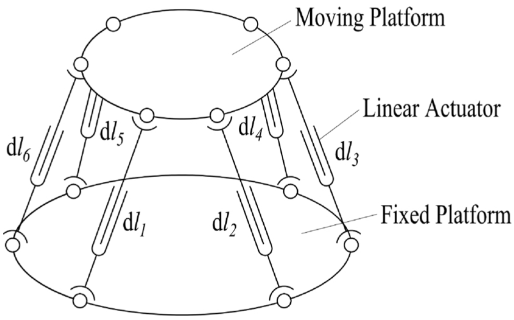

Fig. 2. Diagram of a co-phasing platform with 6 DOF rigid body motion.

surface, at least a five DOF platform is needed to compensate these errors. Parallel mechanism has been the first choice for the co-phasing platform, because of its properties of compact structure, little space occupation, high structural stiffness, large carrying capacity, little error accumulation and high precision.

Fig. 2 shows a typical six DOF parallel platform. It consists of fixed platform, moving platform and six linear actuators. The segment is mounted to the moving platform. Therefore, the segment pose errors are equivalent to the platform positioning errors. Sources of platform positioning errors mainly include fit clearance, creeping phenomenon and control error. They will result in that the moving platform stops at undetermined position and with undetermined attitude. This randomness of positioning errors will lead to slight changes in the other five DOF, even though the platform just moves along one DOF. According to practical experience, positioning errors of the platform approximatively follow multidimensional independent uniform distribution:

$$\Delta X_i \sim \mathrm{U}[a_i, b_i] \tag{2}$$

where ΔX^i is one DOF pose error of the segment defined in its local coordinate system (LCS). a_i and b_i are the error limits.

4. Wavefront deformation originating from co-phasing errors

4.1. Basic theory

The nominal conic-section surface defined in Cartesian coordinate system is shown in Fig. 3 and can be expressed as:

$$z = \frac{cr^2}{1 + \sqrt{1 - (1 + k)c^2r^2}} \tag{3}$$

where $r^2 = x^2 + y^2$. $c = 1/R$ is the paraxial curvature. R is the paraxial ROC. k is conic constant.

An incident ray reflected by a segment with co-phasing errors is sketched in Fig. 4.

The ray with direction $\hat{i}$ originating at point P_1 on the nominal wavefront. It intersects the nominal surface at point P_2, and the actual surface with deformation at point P_3. The reflected ray directions are $\hat{r}_{nom}$ and $\hat{r}$ respectively. When the ray directions are close enough to the PM principal axis vector, the small-angle approximation holds [23], and the total optical path-length difference (OPD) caused by segments slight deformations is the sum of the changes in the incident-ray and reflected-ray OPD:

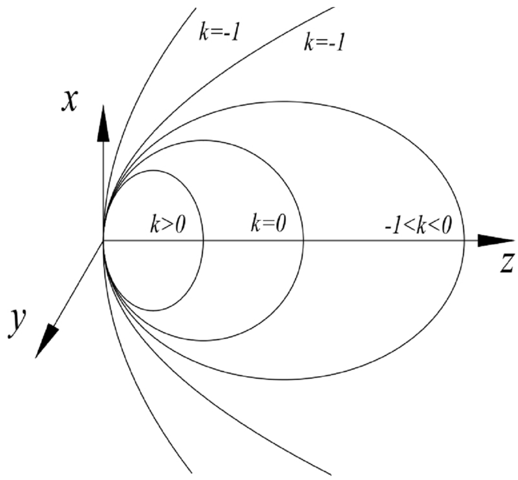

Fig. 3. An incident ray is reflected by a segment with co-phasing errors.

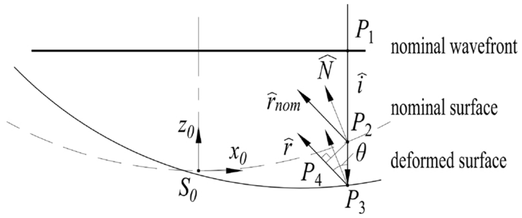

Fig. 4. The OPD originating from pose errors.

$$OPD = \mathrm{d}L(1 + \cos\theta) \tag{4}$$

where $\mathrm{d}L$ is the path length from P_2 to P_3 along the incident ray, θ is the supplementary angle between the incident ray and the reflected ray.

4.2. Wavefront deformation originating from segment pose errors

Set the vector of segment pose errors is:

$$\Delta X = [\Delta\theta_{seg\_x}, \Delta\theta_{seg\_y}, \Delta\theta_{seg\_z}, \Delta s_{seg\_x}, \Delta s_{seg\_y}, \Delta s_{seg\_z}]^T \tag{5}$$

where $\Delta\theta_{seg\_x}$, $\Delta\theta_{seg\_y}$ and $\Delta\theta_{seg\_z}$ are the rotation errors around x, y and z axes of the segment LCS $\{S_i\}$ respectively, and Δs_{seg_x}, Δs_{seg_y} and Δs_{seg_z} are the position errors along x, y and z axes respectively.

According to the homogeneous transformation theory, the actual pose of segment S_i with pose errors can be expressed as:

$$^{Si}T = \begin{bmatrix} R & S \\ 0 & 1 \end{bmatrix} \tag{6}$$

where ^{Si}T is the pose matrix of segment S_i defined in its LCS $\{S_i\}$. $S = [\Delta s_{seg\_x}, \Delta s_{seg\_y}, \Delta s_{seg\_z}]^T$ is the position vector.R is the attitude matrix and can be derived by rotation transformations (including roll, pitch and yaw):

$$\begin{aligned} R &= \mathrm{RPY}(\Delta\theta_{seg\_z}, \Delta\theta_{seg\_y}, \Delta\theta_{seg\_x}) \\ &= \mathrm{Rot}(z_{seg}, \Delta\theta_{seg\_z})\mathrm{Rot}(y_{seg}, \Delta\theta_{seg\_y})\mathrm{Rot}(x_{seg}, \theta_{seg\_x}) \end{aligned} \tag{7}$$

where $\mathrm{Rot}(x_{seg}, \Delta\theta_{seg\_x})$ means rotation $\Delta\theta_{seg\_x}$ around the x-axis of segment LCS, $\mathrm{Rot}(y_{seg}, \Delta\theta_{seg\_y})$ means rotation $\Delta\theta_{seg\_y}$ around the y-axis of segment LCS, and $\mathrm{Rot}(z_{seg}, \Delta\theta_{seg\_z})$ means rotation $\Delta\theta_{seg\_z}$ around the z-axis of segment LCS:

$$\mathrm{Rot}(x_{seg}, \Delta\theta_{seg\_x}) = \begin{bmatrix} 1 & 0 & 0 \\ 0 & \cos\Delta\theta_{seg\_x} & -\sin\Delta\theta_{seg\_x} \\ 0 & \sin\Delta\theta_{seg\_x} & \cos\Delta\theta_{seg\_x} \end{bmatrix} \tag{8}$$

$$\mathrm{Rot}(y_{seg}, \Delta\theta_{seg\_y}) = \begin{bmatrix} \cos\Delta\theta_{seg\_y} & 0 & \sin\Delta\theta_{seg\_y} \\ 0 & 1 & 0 \\ -\sin\Delta\theta_{seg\_y} & 0 & \cos\Delta\theta_{seg\_y} \end{bmatrix} \tag{9}$$

$$\mathrm{Rot}(z_{seg}, \Delta\theta_{seg\_z}) = \begin{bmatrix} \cos\Delta\theta_{seg\_z} & -\sin\Delta\theta_{seg\_z} & 0 \\ \sin\Delta\theta_{seg\_z} & \cos\Delta\theta_{seg\_z} & 0 \\ 0 & 0 & 1 \end{bmatrix} \tag{10}$$

The effect of segment pose errors on the reflected-ray position is:

$$\begin{bmatrix} ^{Si}P'_2 \\ 1 \end{bmatrix} = {}^{Si}T \begin{bmatrix} ^{Si}P_2 \\ 1 \end{bmatrix} \tag{11}$$

where $^{Si}\circ$ is a vector defined in LCS $\{S_i\}$. $P_2 = [x_2, y_2, z_2]^T$ is the intersection of the incident-ray and the nominal surface. $P'_2 = [x'_2, y'_2, z'_2]^T$ is the point on the actual surface corresponding to P_2 (Fig. 5).

The position vector of point P'_2 defined in globe coordinate system (GCS) $\{S_0\}$ is:

$$\begin{bmatrix} ^{S0}P'_2 \\ 1 \end{bmatrix} = {}^{S0}_{Si}T \begin{bmatrix} ^{Si}P'_2 \\ 1 \end{bmatrix} = {}^{S0}_{Si}T\,{}^{Si}T \begin{bmatrix} ^{Si}P_2 \\ 1 \end{bmatrix} \tag{12}$$

where $^{S0}\circ$ is a vector defined in GCS $\{S_0\}$, and $^{S0}_{Si}T$ is the transfer matrix from the GCS $\{S_0\}$ to the LCS $\{S_i\}$.

The OPD due to segment pose errors in incident-ray is :

$$\mathrm{d}L_1 = \overrightarrow{P_2''P_2'}\cdot\hat{i} \tag{13}$$

where P_2'' is the intersection of the nominal surface and the incident-ray which passes through point P'_2 and is along direction $\hat{i}$.

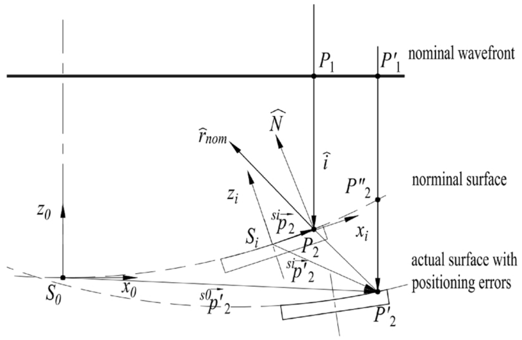

Fig. 5. The OPD originating from aspheric parameter errors.

According to Eq. (4), the total OPD due to slight segment pose errors is:

$$OPD_1 = \mathrm{d}L_1(1 + \cos\theta) \tag{14}$$

4.3. Wavefront deformation originating from aspheric parameters errors

The aspheric parameter errors ΔR and Δk do not change the surface rotational symmetry, and the actual optical surface can be expressed as:

$$Sag'(r) = \frac{c'r^2}{1 + \sqrt{1 - (1 + k')c'^2r^2}} \tag{15}$$

where $c' = 1/(R + \Delta R)$ and $k' = k + \Delta k$.

The effect of segment parameter errors on the OPD is much the same as the effect of segment pose errors: surface deformation changes the OPD in incident-ray:

$$\mathrm{d}L_2 = \overrightarrow{P_2P_3}\cdot\hat{i} \tag{16}$$

Where P_2 is the intersection of the incident-ray and nominal surface, and P_3 is the intersection of the incident-ray and actual surface (Fig. 6).

Therefore, the total OPD due to slight aspheric parameter errors is:

$$OPD_2 = \mathrm{d}L_2(1 + \cos\theta) \tag{17}$$

5. Numerical simulation

Extensive numerical simulations were performed to validate Eqs. (14) and (17). Using 1037 incident-rays, which are approximately uniformly distributed on each segment surface, calculates partial WD. The total PM WD is the sum of all 1037n (n is the segments number) incident-rays OPD:

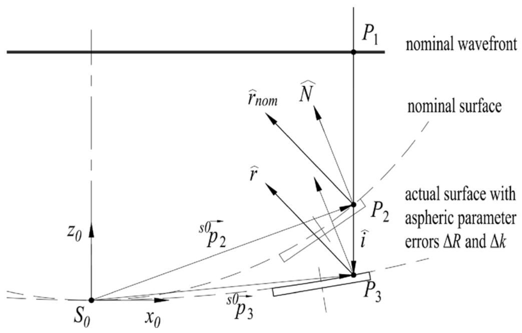

Fig. 6. The incident-rays position.

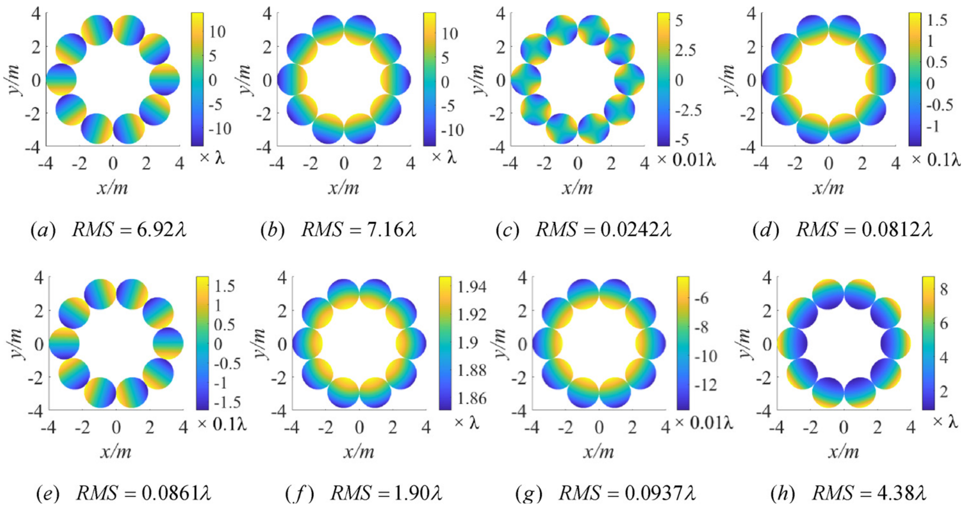

Fig. 7. The WD originating from single co-phasing error with definite value.

$$\Delta w = \begin{bmatrix} OPD_{ray\_1} \\ OPD_{ray\_2} \\ \vdots \\ OPD_{ray\_1037n} \end{bmatrix} \tag{18}$$

5.1. Simulations of co-phasing errors with definite value

For definite segment co-phasing errors, the accurate wavefront deformation (WD) can be obtained through numerical simulation (Fig. 7). Fig. 7(a)–(c) are respectively the WDs with three DOFs ($\Delta\theta_{seg\_x}$, $\Delta\theta_{seg\_y}$, $\Delta\theta_{seg\_z}$) attitude error 1″. Fig. 7(d)–(f) are respectively the WDs with three DOFs (Δs_{seg_x}, Δs_{seg_y}, Δs_{seg_z}) position error $1\lambda(\lambda = 632.8nm)$. Fig. 7(g) is the WD with the paraxial ROC error $\Delta R = 1\lambda$. Fig. 7(h) is the WD with the conic constant error Δk = 1e-4. It can be seen from Fig. 7 that each segment has the same WD in its own LCS, and the segmented PM has rotational symmetry wavefront aberration in its own PM coordinate system (GLS). Moreover, the segments low-order aberrations compose the PM high-order aberration. These plots verify that the Eqs. (14), (17) and (18) are able to calculate the impacts of all segment co-phasing errors defined in LCS.

The WD root mean square (RMS) changing with single co-phasing error limit is shown in Fig. 8, the abscissa of which uses normalized coordinate. The attitude errors limits change from 0° to 0.5°, the position errors limits change from 0 mm to 1 mm, the paraxial ROC error limit changes from 0 mm to 2 mm, and the conic constant error limit changes from 0 to 0.01. It can be seen from the sensitivity curves that the PM WD changes linearly with co-phasing errors when the errors limits are small enough, which is defined as the linearity theorem. Moreover, the WD sensitivity to different co-phasing error is disparate.

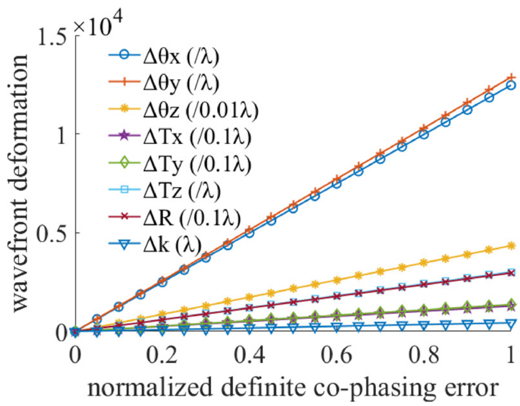

Fig. 8. Sensitivity curves of the WD RMS changing with single co-phasing error.

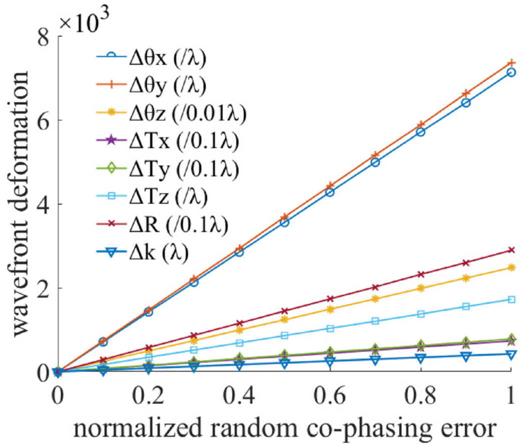

Fig. 9. Sensitivity curves of WD RMS expectation changing with single random co-phasing error.

5.2. Simulations of single random co-phasing error

In fact, each segment has disparate co-phasing error, the value of which is random and follows certain statistical regularity. Using the Monte Carlo simulations, the WD probability distribution can be obtained, and the WD expectation and standard variance can be predicted. These data can evaluate the impact of random co-phasing errors approximately. Fig. 9 shows the WD RMS expectation changing with single random co-phasing error, and Fig. 10 shows the WD RMS standard variance changing with single random co-phasing error. Similarly, normalized abscissa is used, and the variation range of each co-phasing error limit is the same as that of Fig. 8. The pose errors follow multidimensional independent uniform distribution, the parameter errors follow multidimensional independent normal distribution, and the sampling times is 10,000 for each Monte Carlo simulation. It can be seen from the results that the expectation of the WD RMS obeys the linearity theorem similarly, and the standard variance also obeys the linearity theorem approximately. Moreover, disparate co-phasing error form has different impact capability.

5.3. Simulations of mixed co-phasing errors

Similarly, all co-phasing errors are coexisting and independent with each other. Fig. 11 shows the WD probability distribution originating from the above eight kinds of random co-phasing errors, where the WD RMS expectation stemming from single co-phasing error is 1λ. It can be seen from the curve (Fig. 11(a)) that the WD obeys normal distribution approximately, and the total WD is the root sum square (RSS) of the WD caused by all single co-phasing error:

$$E_{rms} = 2.85\lambda \approx \sqrt{\sum_{i=1}^{8} RMS_i} = \sqrt{8\lambda^2} = 2.83\lambda \tag{19}$$

where E_{rms} is the expectation of total WD RMS, and RMS_i is the WD RMS expectation stemming from single co-phasing error. Fig. 11(b) shows the average WD map. Because positive OPD compensates negative OPD, the RMS of the map is approximately zero,

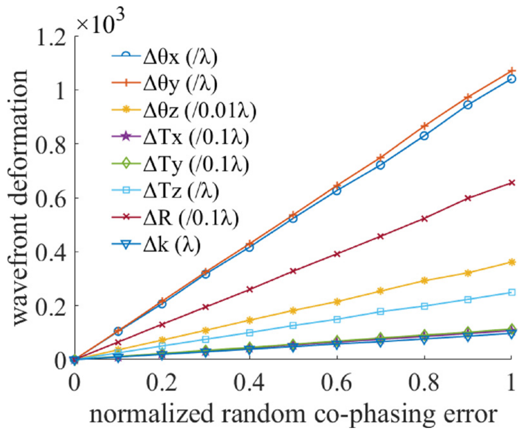

Fig. 10. Sensitivity curves of WD RMS standard variance changing with single random co-phasing error.

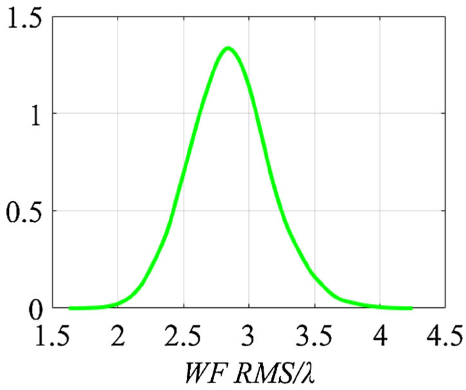

(a) WD RMS probability distribution

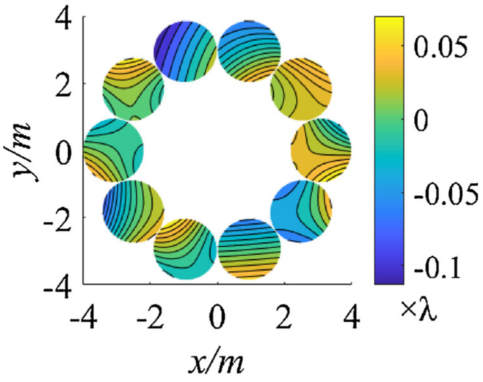

(b) Average WD

Fig. 11. WD originating from mixed random co-phasing errors.

which is consistent with that the best expectations of all co-phasing errors is zero.

6. Conclusion

This paper proposes a nonlinear method for calculating the WD stemming from segments random pose and aspheric parameter errors. Taking an 8 m segmented PM composed by 10 segments for instance, numerical simulations are accomplished. Our research shows that random co-phasing errors will lead to uncertain WD which can be estimated using the Monte Carlo simulation. When the error limit is small enough, the WD caused by definite or random co-phasing errors approximately obeys the linearity theorem, and the total WD is the root sum square of WD generated by all single co-phasing errors.

Acknowledgments

This work was supported by the National Key Technologies R&D Program of China (Grant No. 2016YFB0500100), Civil aerospace pre-research project (Grant No.D040101), Equipment pre-research project (Grant No.30502010501HT01), National Natural Science Foundation of China (Grant No.11873007).

References

[1] J.M. Oschmann, et al., Special section guest editorial: space telescopes, Opt. Eng. 52 (9) (2013) 091801, , https://doi.org/10.1117/1.OE.52.9.091801.
[2] J.S. Fender, Future trends in large space optics, Proc. SPIE 4013 (2000) 682–686, https://doi.org/10.1117/12.394005.
[3] N. Rioux, et al., A future large-aperture UVOIR space observatory: reference designs, Proc. SPIE 9602 (2015) 960205, , https://doi.org/10.1117/12.2187758.
[4] D.C. Redding, et al., Beyond JWST: performance requirements for a future large UVOIR space telescope, Proc. SPIE 9143 (2014) 914312, , https://doi.org/10.1117/12.2056568.
[5] C.F. Lillie, Large deployable telescopes for future space observatories, Proc. SPIE 5899 (2005) 58990D, , https://doi.org/10.1117/12.624231.
[6] H.P. Stahl, et al., Potential astrophysics science missions enabled by NASA's planned Ares V, Proc. SPIE 7436 (2009) 743607, https://doi.org/10.1117/12.826748.
[7] H.S. Yang, et al., Technology and development of deployable segmented ultra-large-aperture space remote sensors, Opt. Precision Eng. 26 (6) (2018) 1287–1298.
[8] C. Atkinson, et al., Status of the JWST optical telescope element, Proc. SPIE 9904 (2016) 990403, https://doi.org/10.1117/12.927594.
[9] M. Postman, et al., Advanced technology large-aperture space Telescope: science drivers and technology developments, Opt. Eng. 51 (1) (2012) 011007, , https://doi.org/10.1117/1.OE.51.1.011007 2012.
[10] J.J. Rey, et al., A deployable, annular, 30m telescope, space-based observatory, Proc. SPIE 9143 (2014) 914318, https://doi.org/10.1117/12.2057182.
[11] A. Jacob, P. Parihar, A co-phasing technique for segmented mirror telescopes, Proc. SPIE 9654 (2015) 96540G, https://doi.org/10.1117/12.2181778.
[12] D. Yue, et al., Co-phasing of the segmented mirror and image retrieval based on phase diversity using a modified algorithm, Appl. Opt 54 (26) (2015) 7917–7924, https://doi.org/10.1364/AO.54.007917.
[13] H. Choi, et al., Simultaneous multi-segmented mirror orientation test system using a digital aperture based on sheared Fourier analysis, Opt. Express 25 (15) (2017) 18152–18164, https://doi.org/10.1364/OE.25.018152.
[14] Z. Liao, et al., Self-calibrating phase measurement based on diffraction theory and numerical simulation experiments, Opt. Eng. 54 (2) (2015) 025116, , https://doi.org/10.1117/1.OE.54.2.025116.
[15] K.N. Yao, et al., Pyramid wavefront sensor using a sequential operation method, Appl. Opt. 54 (13) (2015) 3894–3901, https://doi.org/10.1364/AO.54.003894.
[16] J.L. Jiang, W.R. Zhao, Phasing piston error in segmented telescopes, Opt. Express 24 (17) (2016) 19123–19137, https://doi.org/10.1364/OE.24.019123.
[17] J.F. Simar, Y. Stockman, J. Surdej, Single-wavelength coarse phasing in segmented telescopes, Appl. Opt. 54 (5) (2015) 1118–1123, https://doi.org/10.1364/AO.54.001118.
[18] G.H. Ju, C.X. Yan, Z.Y. Gu, Elimination of the field-dependent aberrations of the JWST-like space telescopes in the multi-field fine-phasing process, Appl. Opt. 56 (10) (2017) 2724–2740, https://doi.org/10.1364/AO.56.002724.
[19] G. Chanan, M. Troy, Strehl ratio and modulation transfer function for segmented mirror telescopes as functions of segment phase error, Appl. Opt. 38 (31) (1999) 6642–6647, https://doi.org/10.1364/AO.38.006642.
[20] J.L. Flores, et al., Effects of misalignment error on the optical transfer functions of synthetic aperture telescopes, Appl. Opt. 43 (32) (2004) 5926–5932, https://doi.org/10.1364/AO.43.005926.
[21] J. Zhang, W.R. Zhao, F. Yang, L.F. Zhang, The effects of piston error on image quality of synthetical aperture optical imaging system, Proc. SPIE 8557 (2012) 85570Z, https://doi.org/10.1117/12.999733.

[22] Z. Liu, et al., Analysis of relationship between far-field images and piston error of synthetic-aperture telescopes for the broadband target wave, Proc.IEEE-2010 OSA-IEEE-cos Advences in Optoelectronics and Micro/Nano-Optics (2011) 1–5, https://doi.org/10.1109/AOM.2010.5713589.
[23] D.C. Redding, W.G. Breckenridge, Optical modeling for dynamics and control analysis, J. Guid. Control. Dyn. 14 (1991) 1021–1032, https://doi.org/10.2514/3.20745.

Huisheng Yang is an assistant researcher at Changchun Institute of Optics, Fine Mechanics and Physics, Chinese Academy of Sciences (CIOMP). He received his BS and MS degrees in mechanical design manufacturing and automation from Harbin Institute of Technology (HIT) in 2007 and 2009. He is the author of more than 10 journal papers and has achieved more than 20 Chinese patents for invention. His current research interests include ultra-large-aperture space remote sensor and ultra-precision mechanical structure.